RSC Advances

ROYAL SOCIETY OF CHEMISTRY

www.rsc.org/advances

Ni Cluster Nucleation and Growth on AnataseTiO_2(101) Surface: A Density Functional Theory Study

Yanxin Wang[1], Yan Su[2], Mingyuan Zhu[1], Lihua Kang[1]*

[1]College of Chemistry and Chemical Engineering/ Key Laboratory for Green Processing of Chemical Engineering of Xinjiang Bingtuan. Shihezi University, Shihezi, Xinjiang, 832000, PR China

[2]School of Physics and Optoelectronic Technology and College of Advanced Science and Technology, Dalian University of Technology, Dalian 116024, China.

Abstracts: Density functional theory (DFT) calculations are carried out to study the nucleation and growth rule of Ni clusters on both perfect and defective anatase TiO_2(101) surface using supported Ni_n (n = 1–6) cluster models. Our results show that a single Ni atom prefers to adsorb at the bridge site formed by two-coordinational oxygen (2cO) atoms on the perfect TiO_2(101) surface and at the 3cO-bridge site on the defective TiO_2(101) surface. The active site for Ni cluster growth on the perfect TiO_2(101) surface shifts from the bridge site of two 2cO atoms or 2cO−6cTi−3cO bridge site for Ni_1, Ni_2, and Ni_3 clusters to the 2cO−5cTi bridge site for Ni_4, Ni_5, and Ni_6. The Ni cluster cohesive energy was maintained constant with cluster size variation on both perfect and defective surface. Ni-TiO_2 interaction is the main driving force of the initial Ni nucleation stage, and Ni-Ni interaction begins to control the Ni_n cluster growth process with increased cluster size.

Keywords: DFT, nucleation, active site, interaction

*Corresponding author E-mail: kanglihua@shzu.edu.cn

Tel:+86-0993-2057213;Fax:+86-0993-2057270

1. Introduction

Transition metal clusters supported on metal-oxide substrates are attracting considerable attention because of their importance in heterogeneous catalysis.[1] A number of studies have indicated that the interaction between metal and support significantly affects the activity and selectivity of catalytic reactions.[2-5] Therefore, understanding metal cluster nucleation and growth on oxide support mechanisms is important to further explore the metal–support interaction and improve the catalytic activity of the systems.

Among the metal-oxide supports, TiO_2 is the most widely used in many processes such as hydrogenation,[6-8] CO oxidization,[9-11] and water splitting.[12-14] The two most common TiO_2 polymorphs are rutile and anatase. Rutile TiO_2 is the most widely studied form both experimentally and theoretically, whereas, anatase TiO_2 has been found to be dominant in nanocrystalline phase.[15] Extensive experimental and theoretical investigations have been performed on metal cluster nucleation and growth pattern, including Au,[16-22] Pt,[23-27] and Pd,[28-33] on both rutile and anatase TiO_2 surfaces.

Recently, some experiment and theoretical studies concerning Ni cluster deposition on rutile TiO_2(110) surfaces have been reported. Chen et al.[34] studied Ni and Cu growth on TiO_2(110) using scanning tunneling microscope (STM). They reported that Ni islands grew three dimensionally at room temperature, and although the Ni-TiO_2 interfacial energy should be greater than that of Cu-TiO_2, the Ni islands did not grow flatter on the surface compared to Cu, indicating that Ni islands were located preferably at step edges with high step edge density. This was further confirmed by the Tanner group's STM study.[35] Asakura and co-workers[36] investigated Ni cluster growth mode and morphology on a TiO_2(110) surface with a wide terrace using low coverage STM. They observed that

many flat and small Ni islands were located on the terrace, not at step edges with low step density. The initial stage bonding structure and binding character of Ni thin-film growth on a rutile (110) surface using first-principle density functional theory were studied by Ellis et al.[37] Their results showed that Ni atoms in the first monolayer were preferentially adsorbed on top of bridging oxygen atoms and upon secondary surface oxygen. The bond strength between Ni adatom and substrate was much stronger than that between Ni adatoms. However, for Ni deposition on anatase TiO_2(101), almost no report was found until J. Chen and co-workers[38] found that nickel catalysts supported on ZrO_2 (monoclinic phase), SiO_2, TiO_2 (anatase phase), and γ-Al_2O_3, Ni/TiO_2 (anatase phase) showed the best catalytic hydrogenation performance of o-chloronitrobenzene to o-chloroaniline. The good Ni/TiO_2 performance was attributed to the strong N=O band polarization induced by TiO_x oxygen vacancies which was produced by high temperature reduction. Therefore, to explore Ni cluster deposition nucleation and growth mechanism deposition on anatase TiO_2(101) surface is essential. Meanwhile, the role of oxygen vacancies on the TiO_2 surface in dispersing and nucleating Ni clusters should be understood.

In the present work, we use anatase TiO_2(101) surface as the oxide support for depositing Ni_n (n = 1–6) clusters. DFT calculations on Ni cluster nucleation and growth mechanism on perfect and defective support surfaces were carried out. This work provides a fundamental understanding to further disclose the metal–support interaction and gives helpful design and synthesis instructions of supported Ni-based catalysts in heterogeneous catalysis.

2. Model catalysts and computational details

The calculated bulk anatase TiO_2 structure lattice constants: a = 3.776 Å, c = 9.486 Å were comparable with experimental data (ICSD #24276). The (101) surface was modeled with 11.33×10.21×17.84 Å dimensions, which included 1×3 sized supercell slab with 12 atomic layers. The vacuum region separating the slabs in the direction perpendicular to the surface was set to 12 Å. The atomic positions of the six uppermost layers were always fully relaxed. In addition, the oxygen vacancy was obtained by removing one surface 2cO atom (marked with green circle in Figure 1b) from the 1×3 surface unit cell, corresponding to 1/6 oxygen vacancy density. The properties of isolated Ni_n clusters were calculated using a 15×15×15Å cubic unit cell. Side (left panel) and top (right panel) view of the anatase TiO_2(101) surface are shown in Figure 1.

The fully periodic plane-wave DFT calculations implemented in the Vienna Ab initio Simulation Program (VASP)[39,40] were employed. DFT calculations were performed with the generalized gradient approximation PW91 function[41] implemented with projector augmented wave function (PAW) [42,43] for representing the non-valence core electrons. For better calculation accuracy, a 2x2x1 k-point grid determined by the Monkhorst-Pack method was used. The plane-wave cutoff energy was optimized at 400 eV. The convergence criteria for electronic self-consistent iteration were set to 1.0×10^{-4}eV, and the atomic positions were optimized by means of a conjugate-gradient algorithm until atomic forces were smaller than 0.02 eV/Å. Spin-polarized calculations were performed to account for the magnetic properties of nickel. Charge distributions were estimated using Bader's atoms in molecules (AIM) theory of using the algorithm developed by Henkelman.[44,45]

To describe the interaction between Ni cluster and titania surface, adsorption energy

is defined as follows:[33]

$$E_{ads} = -[E(Ni_n/TiO_2) - E(TiO_2) - E(Ni_n)] \quad (1)$$

where n is the total number of absorbed Ni atoms; $E(Ni_n/TiO_2)$, $E(TiO_2)$, and $E(Ni_n)$ are the total energies of the TiO_2 substrate with Ni_n cluster, the bare TiO_2 substrate, and the free Ni_n cluster in the gas phase, respectively.

3. Results and discussion

3.1 Perfect and defective TiO_2(101) surface

Anatase TiO_2(101) surface presents a stepped structure, as shown in Figure 1. 3-fold-coordinational oxygen atoms (3cO) and 6-fold-coordinational titanium atoms (6cTi) were fully saturated whereas the 2cO and 5cTi atoms were coordinately unsaturated (these atoms are marked with black arrows in the side and top views of the surface in Figure 1). After optimization, atomic positions of the six uppermost layers changed. The 3cO and 6cTi atoms rose by 0.41 and 0.21 Å, respectively, and the 2cO and 5cTi by 0.12 and 0.03 Å, respectively, relative to their bulk position. However, the 2cO-6cTi and 2cO-5cTi bond lengths shortened by 0.05 and 0.13 Å, respectively.

The oxygen vacancy was obtained by removing a bridging 2cO atom from a (1×3) surface supercell (vacancy coverage = 1/6 ML). Oxygen vacancy produced gave rise to significant structure relaxations and important changes of the electronic properties (changes of the electronic properties will be shown in 3.2.3 section). The original 6cTi and 5cTi atoms bound to the 2cO atom at the vacancy site become five- and four-coordinational, denoted as $Ti_{v\text{-}5c}$ and $Ti_{v\text{-}4c}$, respectively. The 3cO atom under the oxygen vacancy relaxed upward by 0.29 Å. $Ti_{v\text{-}5c}$ and $Ti_{v\text{-}4c}$ relaxed inward by 0.06 and 0.09 Å, respectively. Both relaxed away from each other, which led to $Ti_{v\text{-}5c}$–3cO–$Ti_{v\text{-}4c}$

angle change from 101.92° to 126.51° on the perfect surface.

The formation energy of an oxygen vacancy was defined with respect to the energy of an oxygen molecule and calculated according to: $E = -[E_{perfect} - E_{defective} - 1/2E_{O2}]$. Our calculated oxygen vacancy formation energy was 4.80 eV. The slab was kept neutral after 2cO was removed, causing some unpaired electrons. Bader charge analysis showed that the excess electrons were mainly localized at the $Ti_{v\text{-}5c}$ and $Ti_{v\text{-}4c}$ atoms.

3.2.1 Single Ni atom adsorption on the perfect and defective surface

Several possible initial adsorption sites for a single Ni adatom on anatase TiO_2(101) surface were tried. After optimization, three stable adsorption structures denoted as $Ni_{1,a}$, $Ni_{1,b}$, $Ni_{1,c}$ as well as their adsorption energies are presented in Figure 2. The description of the structures ($Ni_{1,b}$, $Ni_{1,c}$) are shown in supporting information. In the most stable structure $Ni_{1,a}$, the Ni atom adsorbed at a bridge site of two edge 2cO atoms (2cO-bridge site) along the [010] direction, with the Ni-2cO bond lengths of ~1.88 Å, respectively. The Ni–2cO bond length was much shorter compared to Pt–2cO (2.06 Å),[26] Pd–2cO (2.06Å),[33] and Ru–2cO (2.05 Å),[46] which led to stronger interaction between Ni and the TiO_2(101) surface. The Ni adsorption energy on TiO_2 surface was 3.03 eV which is much larger than the reported noble metal atom (0.39eV for Au,[22] 2.84 eV for Pt,[26] and 2.67 eV for Pd[33]) and smaller compared to the Ru atom (3.59eV)[46] on the TiO2(101) surface. The isolated Ni, Au, Pd, Pt and Ru electronic configurations can explain the differences in adsorption mechanisms and energies. They possess different electronic structures with different electron distribution at the d and s levels. Gas phase Ni has a $3d^8 4s^2$ electronic configuration whereas Au, Pd, Pt and Ru have a $5d^{10}6s^1$, $4d^{10}$, $5d^9 6s^1$ and $4d^7 5s^1$ electronic configuration, respectively. Ni has an emptier d band compared to Au, Pd, Pt

and thus has more flexibility to create electronic interactions with the ions of the surface. Therefore, Ni has a stronger binding energy with the surface. Due to the emptiest d band of Ru, it has the strongest binding energy with the surface.

Six possible single Ni adatom adsorption sites on the defective TiO_2(101) surface have been searched. The relaxed structures ($Ni_{1,A}$ and $Ni_{1,B}$) and their adsorption energies are shown in Figure 3. The description of $Ni_{1,B}$ is shown in supporting information. Completely different from Au, Pt and Pd,[22,26,33] the preferable adsorption site for the Ni adatom on the defective surface was not the oxygen vacancy, but the bridge site of two 3cO atoms, with the Ni–3cO bond lengths of 1.87 (left) and 1.89 Å (right), respectively. Ni insertion in the middle of two 3cO atoms pulled these two 3cO atoms close to each other by 0.13 Å, and the right 3cO moved to left by 0.14 Å compared to the clean surface. The 3cO atom movement weakened the 3cO bond strength with its left and right side Ti atoms (Ti^a and Ti^b, respectively), and especially the interaction force of 3cO-Ti^b was nearly zero. The interaction between the Ni adatom and the remaining 2cO atom was much weaker than that in the perfect surface with the Ni-2cO bond length of 2.02 Å. The adsorption energy of Ni_{1A} was 3.10 eV, which is a little higher than the 3.03 eV of Ni_{1a} in the perfect surface.

3.2.2 Density of states and bader charge analysis of the two structure kinds

The total density of state (DOS) plots for the clean perfect and defective TiO_2(101) as well as $Ni_{1,a}$ and $Ni_{1,A}$ are shown in Figure 4. The Fermi level of the clean perfect anatase TiO_2(101) surface is at the top of the valence band. After Ni adsorbed at the perfect anatase (101) surface, the Fermi level moved to the bottom of the conduction band and the band gap was partly filled by the Pd states, which are almost Pd 4d-state contributions. Similarly, Creation of a surface oxygen vacancy also shifted the Fermi level to the

conduction band, indicating the electrons left behind by removing a neutral oxygen atom fill the antibonding orbitals. At the same time, the position of the Fermi level did not change after Ni adsorption at the oxygen vacancy. The Pd states induced not only in the band gap but also at the top of the valance band.

To gain further insight of the bonding nature between the supported Ni adatom and the TiO_2 support, Bader charge analysis was conducted. The Bader charges of $Ni_{1,a}$ and the surface atoms which are directly associated with the Ni adatom on the perfect anatase TiO_2(101) surface, are shown in Table 1S (in the supporting information). The Ni atom was positively charged with a charge of 0.55e, suggesting charge transfer occurrence from the Ni atom to the TiO_2 surface. After Ni atom adsorption on the TiO_2 surface, $2cO^1$, $2cO^2$, $3cO^1$ and $3cO^2$ atoms that directly bonded to Ni atom became more negative owing to receiving a charge of 0.11e, 0.11e, 0.03e and 0.02e, respectively, while 5cTi and 6cTi atoms became less positive. This indicated further that all Ti and O atom types which directly interact with Ni atoms, are all electron receptors. Furthermore, the amounts of charge order transferred from Ni to 2cO, 3cO, and Ti atoms were consistent to their bond strengths. The Ni–2cO bond length was the shortest compared to Ni–Ti and Ni–3cO, which means the strongest bond strength, hence, $2cO^1$ and $2cO^2$ gained the most charge amount (both 0.11 e) from Ni atom. The results indicate that the interaction between Ni atom and the surface TiO_2 atoms was formed via the electron transported among them.

The $Ni_{1,A}$ and $Ni_{1,B}$ atom net charge analysis and of their adjacent atoms with defective surface, is shown in Table 2S and Table 3S, respectively (in the supporting information). With the same situation as Table 1S, $Ni_{1,A}$ was also an electron donor of the defective surface and the net charges were not equally distributed among all atoms

bonded with $Ni_{1,A}$. Surprisingly, although Ni–$3cO^a$ and Ni–$3cO^b$ bond strengths are the strongest, the charge amount $3cO^a$ obtained was less than that of 2cO, $Ti_{v\text{-}5c}$, and $Ti_{v\text{-}4c}$ atom gains, while the charge density of $3cO^b$ was almost constant. From the previous analysis, we know that Ni insertion pulls $3cO^a$ and $3cO^b$ atoms close together resulting to $3cO^a$-Ti^a and $3cO^b$-Ti^b bond strength weakening. Therefore, in addition to charge amount from Ni atom, $3cO^a$ and $3cO^b$ atoms can only accept less charge amounts from Ti^a and Ti^b, respectively, after $Ni_{1,A}$ disposition on the defective TiO_2(101) surface. In spite of higher adsorption energy of $Ni_{1,A}$ than $Ni_{1,a}$ on the TiO_2(101) surface, $Ni_{1,A}$ atom transfers less charge amount (0.35e) compared to $Ni_{1,a}$. No direct correlation between the stability of the configuration and the amount of charge that is transferred was apparent. When the $Ni_{1,B}$ occupied the oxygen vacancy site, it was negatively charged with a charge of -0.29e, indicating that some charges were transferred from the TiO_2(101) surface to Ni atom. Moreover, the Ni atom deposition on the TiO_2 surface resulted in charge density increase on the $Ti_{v\text{-}5c}$ and $Ti_{v\text{-}4c}$ atoms and charge density decrease on the 3cO atom (marked with $3cO^v$ in Figure 3b) under the oxygen vacancy and 3cO atoms (marked with $3cO^1$, $3cO^2$, $3cO^3$ and $3cO^4$ in Figure 3b) directly bound to $Ti_{v\text{-}5c}$ and $Ti_{v\text{-}4c}$ atoms. Therefore, Ni atom interaction with the defective surface was similar to a back-donation interaction[47] where the Ni metal promotes a charge transfer from the surface oxygen to the $Ti_{v\text{-}5c}$ and $Ti_{v\text{-}4c}$ atoms.

3.3 Adsorption of Ni_2 on the perfect and defective surface

After searching different possible sites for Ni dimer adsorption on perfect anatase TiO_2(101) surface, four stable structures denoted as $Ni_{2,a}$ $Ni_{2,b}$ $Ni_{2,c}$ and $Ni_{2,d}$ as well as their adsorption energies were obtained and they are shown in Figure 5. $Ni_{2,b}$ $Ni_{2,c}$ and

$Ni_{2,d}$ are described in supporting information. The Ni–Ni bonds are parallel to the TiO_2(101) surface in all four structures. $Ni_{2,a}$ was built by adding the second Ni atom to the most stable single Ni adsorption ($Ni_{1,a}$) and allowing the structures to relax again. It presents the most stable structure with a Ni atom located at the 2cO bridge site, another Ni adatom adsorbed at the 2cO–6cTi–3cO bridge site. The Ni1–Ni2 distance was 2.56 Å, which is significantly longer than the 2.09 Å of the calculated gas-phase Ni dimer. Combined with various single Ni atom adsorption energies on different surface sites, it can be concluded that the decreasing sequence for Ni adsorption active site is 2cO bridge site, 2cO–6cTi–3cO bridge site, and 2cO-5cTi bridge site.

Three stable adsorbed structures of Ni dimer on defective TiO_2 surface as well as their adsorption energies were obtained, namely, $Ni_{2,A}$, $Ni_{2,B}$, $Ni_{2,C}$ and they are shown in Figure 6. The description of $Ni_{2,B}$, $Ni_{2,C}$ are presented in supporting information. The preferable Ni dimer adsorption sites on defective TiO_2(101) surface are shown in Figure 5a, wherein Ni1 adatom is located at the oxygen vacation, and Ni2 sites are in between Ni1 and one nearby 2cO site. Moreover, Ni2 atom preferred a slight displacement to the left of Ni1 atom thus Ni2 atom has no interaction with its neighboring right 3cO atom. The Ni1–Ni2 bond length was 2.27 Å, which is much shorter than that of Ni_2 on a perfect surface, but is longer than the Ni–Ni bond (2.09 Å) in the gas-phase. This indicates stronger interaction of Ni1and Ni2 in defective surface than in the perfect surface. The adsorption energy of $Ni_{2,A}$ was 3.81eV, which is higher by about 0.80 eV than that of the Ni dimer on a perfect surface. However, this most stable Ni dimer structure adsorbed on the defective TiO_2(101) surface is different from the adsorbed Au dimer and Pd dimer,[22,33] but similar with the Pt dimer.[27]

3.4 Ni_3 adsorption on the perfect and defective surface

Two kinds of Ni trimer structures at the gas phase were considered (i.e., linear and triangular configurations) as the initial states absorbed on the perfect surface. The configurations of $Ni_{3,a}$, $Ni_{3,b}$, $Ni_{3,c}$, $Ni_{3,d}$ as well as their adsorption energies were determined in Figure 7. The description of$Ni_{3,b}$, $Ni_{3,c}$ and $Ni_{3,d}$ are shown in in supporting information. $Ni_{3,a}$, the most stable adsorption configurations, was obtained by adding a third Ni adatom to the $Ni_{2,b}$ structure, in which two Ni atoms symmetrically occupied 2cO–6cTi–3cO bridge sites. The third Ni atom was bound at the 2cO-bridge site and the plane formed by these three Ni atoms was almost parallel with the TiO_2 terrace. The Ni1–Ni2, Ni1–Ni3 and Ni2–Ni3 bond lengths were 2.50, 2.45 and 2.46 Å, respectively. The Ni1–Ni2 bond parallel to the 2cO–2cO bond was slightly longer than the other two Ni–Ni bonds, but shorter compared to the dimer $Ni_{2,d}$, indicating Ni3 adatom strengthens the interaction between Ni1 and Ni2 atoms. The stability order of these Ni_3 trimers on the perfect anatase TiO_2(101) surface further demonstrated that the 2cO–6cTi–3cO bridge site was much more active than the 2cO–5cTi bridge site for Ni cluster adsorption.

Various possible Ni_3 adsorptions (triangular and linear) on the defective anatase TiO_2(101) surface were investigated. Four Ni_3 stable adsorption structures ($Ni_{3,A}$, $Ni_{3,B}$, $Ni_{3,C}$ and $Ni_{3,D}$) as well as their adsorption energies were determined and they are shown in Figure 8. The description of $Ni_{3,C}$ and $Ni_{3,D}$ are shown in supporting information. $Ni_{3,A}$ and $Ni_{3,B}$ were the most stable structures with similar adsorption energies (4.79 and 4.74 eV, respectively). $Ni_{3,A}$ resulted from relaxing initial structures constructed from adding a third Ni atom over the $Ti_{v\text{-}5c}$ atom of $Ni_{2,B}$. In this structure, the Ni3 atom rose above the surface with Ni3-$Ti_{v\text{-}4c}$ distance of 2.35 Å, which made the triangle plane almost

perpendicular to the terrace of TiO_2(101) surface. The Ni1–Ni2, Ni1–Ni3, and Ni2–Ni3 bond lengths were 2.46, 2.28 and 2.26 Å, respectively. $Ni_{3,B}$ was obtained based on $Ni_{2,B}$ by adding a third atom on the 3cO and $Ti_{v\text{-}5c}$ bridge site. The Ni_3 triangle was almost parallel to the TiO_2(101) terrace and the Ni1–Ni2, Ni1–Ni3, and Ni2–Ni3 lengths were 2.46, 2.29 and 2.29 Å, respectively. In contrast to $Ni_{2,A}$ dimer, the Ni1–Ni2 length was elongated by 0.19 Å with the Ni3 atom in both $Ni_{3,A}$ and $Ni_{3,B}$ structure.

3.5 Ni_4, Ni_5, and Ni_6 adsorptions on the perfect and defective surface

Both 2D and 3D structures of Ni_n (n=4, 5, and 6) and their different possible adsorption sites on the perfect anatase TiO_2(101) surface have been searched. Three stable Ni_4 configurations and the most stable Ni_5 and Ni_6 structures, and their adsorption energies are shown in Figure 9. The description of $Ni_{4,b}$ and $Ni_{4,c}$ are shown in supporting information. Ni_4 cluster most preferred a tetrahedral structure (Figure 8a) by adding the fourth Ni atom on top of the triangle Ni plane based on the configuration of $Ni_{3,c}$. Interestingly, the Ni trimer active sites grown to Ni tetrahedron on the perfect anatase TiO_2(101) surface was shifted. Ni_3 would likely grow based on the 2cO-6cTi-3cO bridge site while Ni_4prefered nucleation at the 2cO-5cTi bridge site. The Ni_5 and Ni_6 clusters both preferred 3D geometries ($Ni_{5,a}$ and $Ni_{6,a}$) than 2D structures and their last atom was introduced based on the Ni_{n-1} geometry.

Various possible 2D and 3D Ni_n (n=4, 5, and 6) cluster structures adsorbed on the defective anatase TiO_2(101) surface, were considered and only the most stable geometries with their adsorption energies are shown in Figure 10. For $Ni_{4,A}$, the geometry can be treated as a combination of $Ni_{3,A}$ and $Ni_{3,B}$ configurations in which Ni1 and Ni2 atoms almost symmetrically distribute two sides of the oxygen vacancy site, Ni3 atom bridges

the 3cO and $Ti_{v\text{-}5c}$ and Ni4 atom binds with $Ti_{v\text{-}4c}$. In $Ni_{5,A}$ configuration, the fifth Ni atom was added right above the Ni1, Ni3, and Ni4 triangular plane. In $Ni_{6,A}$, Ni4 and Ni5 atoms symmetrically occupied two sides of $Ti_{v\text{-}4c}$ while other atoms were nearly distributed at the same sites as those of $Ni_{4,A}$. Ni_n (n=4, 5, and 6) clusters on the defective surface also tended to present 3D geometries. As atom number increased, the Ni_n cluster transformed from 2D (n<4) to 3D geometry (n=4, 5, and 6) on both perfect and defective anataseTiO_2(101) surfaces, which has similar trend to that of Pd and Ru clusters on the TiO_2(101)surface.[33,46]

3.6 Ni cluster nucleation and growth rule on anatase TiO_2 (101) surface

According to the various geometry of Ni_n (n = 1–6) stable adsorption on the perfect and defective TiO_2(101) surfaces, we made some conclusions: A single Ni atom prefers to adsorb at the 2cO–bridge site on the perfect TiO_2(101) surface, and 3cO–bridge site on the defective TiO_2(101) surface, whereas the oxygen vacancy is the most active site for Au, Pt and Pd deposition on the defective surface.[22,27,33] Furthermore, a single Ni atom prefers 2cO–bridge site rather than 2cO–5cTi bridge site, and the Ni atoms of Ni_2 and Ni_3 clusters both prefer to occupy the 2cO–bridge site or 2cO–6cTi–3cO bridge site on the perfect TiO_2(101) surface. However, when n was greater than four, the Ni_n growth was based on the 2cO–5cTi bridge site. For Ni_n (n = 1–6) clusters on the defective TiO_2(101) surface, the nucleation site was constant with Ni atoms bridging two 3cO atoms. Like Pd and Ru clusters,[33,46] the adsorbed Ni_3 clusters prefer to form planar triangles and the adsorbed Ni_4, Ni_5 and Ni_6 clusters tend to three-dimensional structures on both perfect and defective TiO_2 surfaces.

To further understand the rule and mechanism of Ni_n clusters nucleation on the

TiO_2(101) surface, the cohesive energy (E_{coh}) is defined in this paper in addition to E_{ads}. The definition of the cohesive energy of adsorbed Ni clusters is as follows:[46]

$$E_{coh} = -[E(Ni_n/ TiO_2)-E(TiO_2)-nE(Ni)] /n \quad (2)$$

where E(Ni) is the total energy of a free Ni atom in the gas phase and n is the number of Ni atoms in the Ni_n clusters. Apparently, $E_{ads} = E_{coh}$ for a single Ni adatom on the surface. E_{coh} represents the ability of metal atoms to grow together on the TiO_2(101) surface. The cohesive energy for Ni_n (n = 1–6) and Au_n (n = 1–3)[22] and Pt_n (n = 1–6)[26,27] as a function of cluster sizes are shown in Figure 11. At the perfect TiO_2 surface, for Pt and Au clusters, E_{coh} increases gradually with the increase of cluster size indicating that the Pt and Au atoms easily form big clusters. By contrast, because their cohesive energy decreased as the size of metal cluster became bigger signifies that when the size of the cluster increased, the advantage of the oxygen vacancy as the nucleation center for Pt and Au clustering was expected to diminish eventually. Compared to Pt and Au clusters, the cohesive energy of Ni clusters was almost kept constant with variation of the cluster sizes both on the perfect and defective surface. Moreover, the clustering energy on the defective surface was greater indicating that the 3cO bridge site of defective surface has some advantages over the bridging 2cO site on the perfect surface as an anchoring site for the adsorbed Ni particle.

What then is the driving force for the growth of Ni clusters? Exploring the definition essence of the cohesive energy, Ni−Ni and Ni−TiO_2 interaction jointly dominated the nucleation behavior of Ni_n clusters. Therefore, we can divide the cohesive energy (E_{coh}) of adsorbed Ni cluster at the perfect and defective TiO_2(101) surface into two parts: one is $E_{Ni\text{-}TiO2}$ and the other one is $E_{Ni\text{-}Ni}$. In addition, the average binding energy of isolated

Ni_n(n = 2–6) clusters, E_{bind} (Ni_n), was introduced. The definition of $E_{Ni\text{-}TiO2}$, $E_{Ni\text{-}Ni}$[33] and E_{bind} (Ni_n)[48] are as follows:

$$E(Ni\text{-}TiO_2) = -[E(Ni_n/TiO_2) - E(TiO_2) - E(Ni_n^*)] /n \quad (3)$$

$$E(Ni\text{-}Ni) = E_{coh} - E_{Ni\text{-}TiO_2} \quad (4)$$

$$E_{bind}(Ni_n) = -[E(Ni_n) - n \times E(Ni)]/n \quad (5)$$

where the $E(Ni_n^*)$ represent the total energy of adsorbed Ni_n cluster (not in the gas phase). E_{bind} is the average Ni−Ni interaction of bare Ni clusters.

The variation of $E_{Ni\text{-}TiO2}$ and $E_{Ni\text{-}Ni}$ of bare and adsorbed Ni_n clusters with the cluster sizes are shown in Figure 12. The interaction between a single Ni atom and both the perfect and defective surface was the strongest and then upon Ni adatom addition, the interactions both gradually weakened. However, the Ni–Ni interactions began to increase from zero to one with Ni atoms in both the perfect and defective surfaces. For Ni_1 and Ni_2 clusters absorbed on the perfect and defective surface, the Ni–TiO_2 interaction was much larger than the Ni–Ni interaction, indicating that the Ni-TiO_2 interaction was the main driving force at the initial stage of Ni nucleation. With regard to Ni_4, Ni_5 and Ni_6 clusters, the Ni–Ni interactions have greatly exceeded the Ni–TiO_2 interaction, showing that the Ni–Ni interaction begins to control the growth process of Ni_n clusters as the cluster size gets larger. This is why Ni_1, Ni_2 and Ni_3 clusters preferably occupy the active sites like 2cO–bridge site or 2cO–6cTi–3cO bridge site, whereas Ni_4, Ni_5 and Ni_6 tend to aggregate at the inactive 2cO–5cTi bridge site to reduce the Ni-TiO_2 interaction. The Ni–Ni interaction for Ni_2 and Ni_3 clusters on the perfect surface was stronger than on the defective surface, while that for Ni_4, Ni_5 and Ni_6 clusters were nearly equal on these two kinds of surfaces. Compared to bare clusters, the perfect surface weakens the strength of

Ni–Ni interaction to a certain degree, whereas the strength would not be affected by the defective surface.

4. Conclusion

First principles DFT calculations were carried out to investigate the energetically stable adsorption structures of Ni_n (n = 1–6) clusters at both perfect and defective anatase TiO_2(101) surface and further disclose the nucleation and growth rule of Ni clusters on these two kinds of surfaces. Our results show that a single Ni atom prefers to adsorb at the 2cO–bridge site on the perfect TiO_2(101) surface, and 3cO–bridge site on the defective TiO_2(101) surface (not the oxygen vacancy). The active site for Ni cluster growth on the perfect TiO_2(101) surface shifted from the bridge site of two 2cO atoms or2cO−6cTi−3cO bridge site for Ni_1, Ni_2 and Ni_3 clusters to the 2cO−5cTi bridge site for Ni_4, Ni_5 and Ni_6. The adsorbed Ni_3 clusters prefer to form planar triangles and the adsorbed Ni_4, Ni_5 and Ni_6 clusters tend to 3D structures on both perfect and defective TiO_2 surfaces.

The cohesive energy of Ni cluster was almost kept constant with variation of the cluster sizes on both the perfect and defective surface. Moreover, the clustering energy on the defective surface was larger than that on the perfect surface. The Ni–TiO_2 interaction was the main driving force at the initial stage of Ni nucleation and the Ni–Ni interaction began to control the growth process of Ni_n clusters as the cluster size gets larger.

Acknowledgements

We gratefully acknowledge the National Natural Science Foundation of China (NSFC, Grant No. 11304208), the National Natural Science Funds of China (NSFC, Grant No. U1203293) and the Ph.D. Programs Foundation of the Xinjiang Production and

Construction Corps (No. 2013BB010).

References

1 V. E. Henrich and P. A. Cox, The Surface Science of Metal Oxides, *Cambridge University Press, Cambridge, U.K,* 1994.

2 P. Castillo-Villalon and J. Ramirez, Spectroscopic Study of the Electronic Interactions in Ru/TiO_2 HDS Catalysts, *J. Catal*., 2009, **268**, 39−48.

3 J. C. Kang, S. L. Zhang, Q. H. Zhang and Y. Wang, Ruthenium Nanoparticles Supported on Carbon Nanotubes as Efficient Catalysts for Selective Conversion of Synthesis Gas to Diesel Fuel, *Angew. Chem., Int. Ed.*, 2009, **48**, 2565−2568.

4 G. N. Vayssilov, Y. Lykhach, A. Migani, T. Staudt, G. P. Petrova, N. Tsud, T. Skala, A.Bruix, F. Illas and K. C. Prince, et al, Support Nanostructure Boosts Oxygen Transfer to Catalytically Active Platinum Nanoparticles, *Nat. Mater.*, 2011, **10**, 310−315.

5 J. Sa, A. Goguet, S. F. R. Taylor, R. Tiruvalam, C. J. Kiely, M. Nachtegaal, G. J. Hutchings and C. Hardacre, Influence of Methyl Halide Treatment on Gold Nanoparticles Supported on Activated Carbon, *Angew. Chem., Int. Ed.*, 2011, **50**, 8912−8916.

6 F. Wang, S. T. Zhang, C. M. Li, J. Liu, S. He, Y. F. Zhao, H. Yan, M. Wei, D. G. Evans and X. Duan, Catalytic behavior of supported Ru nanoparticles on the (101) and (001) facets of anatase TiO_2, *Rsc Adv.*, 2014, **4**, 10834-10840.

7 C.Torres, C. Campos, J. L. G. Fierro, M. Oportus and P. Reyes, Nitrobenzene Hydrogenation on Au/$TiO_2$and Au/SiO_2 Catalyst: Synthesis, Characterization and Catalytic Activity, *Catal. Lett.*, 2013, **143**, 763-771.

8 K. Sun, M. Kohya, S. Tanaka, and S. Takeda, A Study on the Mechanism for H2 Dissociation on Au/TiO_2 Catalysts, *J. Phys. Chem. C*, 2014, **118**, 1611–1617.

9 Y. G. Wang, Y. Yoon, V. A. Glezakou, J. Li and R. Rousseau, The Role of Reducible Oxide–Metal Cluster Charge Transfer in Catalytic Processes: New Insights on the Catalytic Mechanism of CO Oxidation on Au/TiO_2 from ab Initio Molecular Dynamics, *J. Am. Chem. Soc.*, 2013, **135**, 10673–10683.

10 I. X. Green, W. J. Tang, M. Neurock, and J. T. Y.Jr, Insights into Catalytic Oxidation at the Au/TiO_2 Dual Perimeter Sites, *Acc. Chem. Res.*, 2014, **47**, 805–815.

11 H. Einaga, N. Urahama, A. Tou and Y. Teraoka, CO Oxidation Over TiO_2-Supported Pt-Fe Catalysts Prepared by Coimpregnation Methods, *Catal. Lett.*, 2014, **144**, 1653-1660.

12 J. G. Yu, L. F. Qi and M. Jaroniec, Hydrogen Production by Photocatalytic Water Splitting over Pt/TiO_2Nanosheets with Exposed (001) Facets, *J. Phys. Chem. C*, 2010, **114**, 13118 – 13125.

13 P. A. DeSario, J. J. Pietron, D. E. DeVantier, T. H. Brintlinger, R. M. Stroudb and D. R. Rolison, Plasmonic Enhancement of Visible-Light Water Splitting with Au-TiO_2 Composite Aerogels, *Nanoscale*, 2013, **5**, 8073-8083.

14 F. Wu, X. Y. Hu, J. Fan, E. Z. Liu, T. Sun, L. M. Kang, W. Q. Hou, C. J. Zhu and H. C. Liu, Photocatalytic Activity of Ag/TiO_2 Nanotube Arrays Enhanced by Surface Plasmon Resonance and Application in Hydrogen Evolution by Water Splitting, *Plasmonics*, 2013, **8**, 501-508.

15 H. Z. Cheng and A. Selloni, Surface and Subsurface Oxygen Vacancies in Anatase $TiO_2$and Differences with Rutile, *Phys. Rev. B*, 2009, **79**, 092101-092101.

16 C. H. Sun and S. C. Smith, Strong Interaction Between Gold and AnataseTiO_2(001) Predicted by First Principle Studies, *J. Phys. Chem. C*, 2012, **116**, 3524−3531.

17 E. Lira, J. Hansen, L. R. Merte, P. T. Sprunger, Z. S. Li, F. Besenbacher, S. Wendt, Growth of Ag and Au Nanoparticles on Reduced and Oxidized Rutile TiO_2(110) Surfaces, *Topics in Catalysis*, 2013, **56**, 1460-1476.

18 Zhang, L.; Cosandey, F.; Persaud, R.; Madey, T. E. Initial Growth and Morphology of Thin Au Films on TiO_2(110). *Surf. Sci.* **1999**, 439, 73-85.

19 R. P. Galhenage, H. Yan, S. A. Tenney, N. Park, G. Henkelman, P. Albrecht, D. R. Mullins and D. A. Chen, Understanding the Nucleation and Growth of Metals on TiO_2: Co Compared to Au, Ni, and Pt, *J. Phys. Chem. C*, 2013, **117**, 7191 − 7201.

20 R. P. Galhenage, S. C. Ammal, H. Yan, A. S. Duke, S. A. Tenney, A. Heyden, and D. A. Chen, Nucleation, Growth, and Adsorbate-Induced Changes in Composition for Co-Au Bimetallic Clusters on TiO_2, *J. Phys. Chem. C*, 2012, **116**, 24616 − 24629.

21 Y. J. Chen, G. H. Tian, K. Pan, C. G. Tian, J. Zhou, W. Zhou, Z. Y. Ren and H. G. Fu, In Situ Controlled Growth of Well-Dispersed Gold Nanoparticles in TiO_2 Nanotube Arrays as Recyclable Substrates for Surface-Enhanced Raman Scattering. *Dalton Trans.*, 2012, **41**, 1020-1026.

22 A. Vittadini, A. Selloni, Small Gold Clusters on Stoichiometric and Defected TiO_2Anatase (101) and their Interaction with CO: A Density Functional Study, *J. Chem. Phys*,2002, **117**, 353−353.

23 X. Y. Pan and Y.J. Xu, Defect-Mediated Growth of Noble-Metal (Ag, Pt, and Pd) Nanoparticles on TiO_2 with Oxygen Vacancies for Photocatalytic Redox Reactions under Visible Light, *J. Phys. Chem. C*, 2013, **117**, 17996 − 18005.

24 X. Q. Gong, A. Selloni, O. Dulub, P. Jacobson and U. Diebold, Small Au and Pt Clusters at the Anatase TiO_2(101) Surface: Behavior at Terraces, Steps, and Surface Oxygen Vacancies, *J. Am. Chem. Soc*,2008, **130**, 370-381.

25 Y. Zhou, C. L. Muhich, B. T. Neltner, A. W. Weimer and C. B. Musgrave, Growth of Pt Particles on the Anatase TiO_2(101) Surface, *J. Phys. Chem. C*, 2012, **116**, 12114−12123.

26 Y. Han, C. J. Liu, Q. F. Ge, Interaction of Pt Clusters with the Anatase TiO_2(101) Surface: A First Principles Study, *J. Phys. Chem. B*, 2006, **110**, 7463−7472.

27 Y. Han, C. J. Liu, Q. F. Ge, Effect of Surface Oxygen Vacancy on Pt Cluster Adsorption and Growth on the Defective Anatase TiO_2(101) Surface, *J. Phys. Chem. B*, 2007, **111**, 16397-16404.

28 C. Xu, X. Lai, G. W. Zajac and D. W. Goodman, Scanning Tunneling Microscopy Studies of the TiO_2(110) Surface: Structure and the Nucleation Growth of Pd, *Phys. Rev. B*, 1997, **56**, 13464-13482.

29 M. D. Negra, N. M. Nicolaisen, Z. Li and P. J. Moller, Study of the Interactions between the Overlayer and the Substrate in the Early Stages of Palladium Growth on TiO_2(110), *Surf. Sci.*, 2003, **540**, 117-128.

30 W. N. Zhao, H. X. Lin, Y. Li, Y. F. Zhang, X. Huang and W. K. Chen, Growth mechanism of palladium clusters on rutile TiO_2(110) surface, *J. Nat. Gas Chem*, 2012, **21**, 544-555.

31 S. V. Ong and S. N. Khanna, Theoretical Studies of the Stability and Oxidation of Pd_n (n = 1–7) Clusters on Rutile TiO_2(110): Adsorption on the Stoichiometric Surface, *J. Phys. Chem. C*, 2012, **116**, 3105 − 3111.

32 J. F. Sanzand A. Marquez, Adsorption of Pd Atoms and Dimers on the TiO_2 (110) Surface: A First Principles Study, *J. Phys. Chem. C*, 2007, **111**, 3949-3955.

33 J. L. Zhang, M. Zhang, Y. Han, W. Li, X. K. Meng and B. N. Zong, Nucleation and Growth of Palladium Clusters on Anatase TiO_2(101) Surface: A First Principle Study, *J. Phys. Chem. C*, 2008, **112**, 19506−19515.

34 J. Zhou, Y. C. Kang and D. A. Chen, Controlling Island Size Distributions: A Comparison of Nickel and Copper Growth on TiO_2(110), *Surf. Sci. Lett.*, 2003, **537**, L429-L434.

35 R. E. Tanner, K. Goldfarb, M. R. Castell and G. A. D. Briggs, The Evolution of Ni Nanoislands on the Rutile TiO_2(110) Surface with Coverage, Heating and Oxygen Treatment, *Surf. Sci.*, 2001, **486**, 167-184.

36 K. Fujikawa, S. Suzuki, Y. Koike, W. J. Chun and K. Asakura, Self-Regulated Ni Cluster Formation on the TiO_2(110) Terrace Studied Using Scanning Tunneling Microscopy, *Surf. Sci.*, 2006, **600**, L117–L121.

37 P. L. Cao, D. E. Ellis and V. P. Dravid, First-principles study of initial stage of Ni thin-film growth on a TiO_2(110) surface, *J. Mater. Res.*, 1999, **14**, 3684-3689.

38 J. Xiong, J. X. Chen and J. Y. Zhang, Liquid-Phase Hydrogenation of O-Chloronitrobenzene over Supported Nickel Catalysts, *Catalysis Communications*., 2007, **8**, 345-350.

39 G. Kresse and J. Furthmuller, Efficient Iterative Schemes for Ab Inition Total-Energy Calulation Using a Plane-Wave Basis Set, *Phys. Rev. B*, 1996, **54**, 11169−11186.

40 G. Kresse and J. Furthmuller, Efficiency of Ab-Inition Total Energy Calulation for Metals and Semi conductors Using a Plane-Wave Basis Set, *Comput. Mater. Sci.*,

1996, **6**, 15−50.

41 J. P. Perdew, J. A. Chevary, S. H. Vosko, K. A. Jackson, M. R. Pederson, D. J. Singh and C. Fiolhais, Atoms, Molecules, Solids, and Surfaces: Applications of the Generalized Gradient Approximation for Exchange and Correlation, *Phys. Rev. B*, 1992, **46**, 6671−6687.

42 P. E. Blochl, Projector Augmented-Wave Method, *Phys. Rev. B*, 1994, **50**, 17953−17979.

43 G. Kresse and D. Joubert, From Ultrasoft Pseudopotentials to the Projector Augmented-Wave Method, *Phys. Rev. B*, 1999, **59**, 1758−1775.

44 E. Sanville S. D. Kenny, R. Smith and G. Henkelman, Improved Grid-Based Algorithm for Bader Charge Allocation, *J. Comput. Chem.*, 2007, **28**, 899-908.

45 G. Henkelman, A. Arnaldsson and H. A. Jonsson, Fast and Robust Algorithm for Bader Decomposition of Charge Density. *Comput, Mater. Sci.*, 2006, **36**, 354-460.

46 S. T. Zhang, C. M. Li, H. Yan, M. Wei, D. G. Evans and X. Duan, Density Functional Theory Study on the Metal−Support Interaction between Ru Cluster and Anatase TiO_2(101) Surface, *J. Phys. Chem. C*, 2014, **118**, 3514−3522.

47 L. G. V. Briquet, C. A. R. Catlow and S. A. French, Comparison of the Adsorption of Ni, Pd, and Pt on the (0001) Surface of α-Alumina, *J. Phys. Chem. C*, 2008, **112**, 18948−18954.

48 S. Nigam and C. Majumder, Growth Pattern of Ag_n (n = 1-8) Clusters on the α-Al_2O_3(0001) Surface: A First Principles Study, *Langmui*r, 2010, **26**, 18776–18787.

Graphic for manuscript

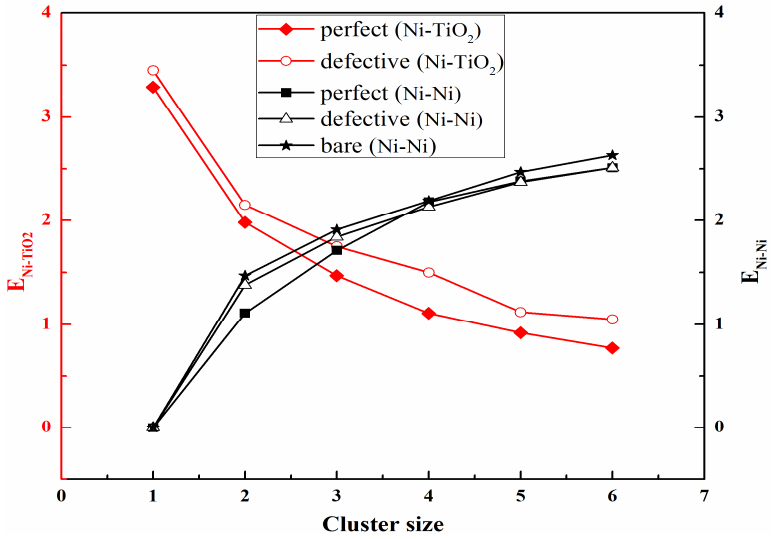

► The paper is the first to study the nucleation and growth rule of Ni clusters on both perfect and defective anatase TiO_2(101) surface.

► A single Ni atom prefers to adsorb at the 2cO-bridge site on the perfect surface, and 3cO-bridge site on the defective surface.

► The active site for Ni cluster growth on the perfect surface shifts from the bridge site of two 2cO atoms or 2cO−6cTi−3cO bridge site to the 2cO−5cTi bridge site.

► The Ni-TiO_2 interaction is the main driving force at the initial stage of Ni nucleation.

► The Ni-Ni interaction begin to control the growth process of Ni_n clusters as the cluster size gets larger.

Figure Captions

Figure 1. Side (a) and top (b) views of anatase TiO_2 (101) supercell. The red is an O atom and the argent is an Ti atom.

Figure 2. Optimized structures of a single Ni adatom and their corresponding adsorption energy on a perfect anatase TiO_2(101) surface: (a) $Ni_{1,a}$; (b) $Ni_{1,b}$; (c) $Ni_{1,c}$. Their corresponding adsorption energy on the surface are also shown in Figure 2.

Figure 3. Optimized structures of a single Ni adatom and their corresponding adsorption energy on a defective anatase TiO_2(101) surface: (a) $Ni_{1,A}$; (b) $Ni_{1,B.}$ Their corresponding adsorption energy on the surface are also shown in Figure 3.

Figure 4. Density of state for the (a) perfect TiO_2(101) surface (top) and $Ni_{1,a}$ (bottom) and (b) defective TiO_2(101) surface (top) and $Ni_{1,A}$(bottom). The local DOS of Ni, which contributes to the total DOS in $Ni_{1,a}$ and $Ni_{1,A}$, is represented in red color.

Figure 5. Adsorption structures and energies of Ni dimer on the perfect anatase TiO_2(101) surface. (a) $Ni_{2,a}$; (b) $Ni_{2,b}$; (c) $Ni_{2,c}$; and (d) $Ni_{2,d.}$

Figure 6. Adsorption structures and energies of Ni dimer on the defective anatase TiO_2(101) surface. (a) $Ni_{2,A}$; (b) $Ni_{2,B}$; (c) $Ni_{2,C.}$

Figure 7. Top (left) and side views (right) of the stable structures and energies for Ni trimer adsorption on the perfect anatase TiO_2(101) surface: (a) $Ni_{3,a}$; (b) $Ni_{3,b}$; (c) $Ni_{3,c}$; (d) $Ni_{3,d}$.

Figure 8. Top (left) and side views (right) of the stable structures and energies for Ni trimer adsorption on the defective anatase TiO_2(101) surface: (a) $Ni_{3,A}$; (b) $Ni_{3,B}$; (c) $Ni_{3,C}$ and (d) $Ni_{3,D}$.

Figure 9. Top (left) and side views (right) of the stable structures and energies for Ni_4, Ni_5 and Ni_6 adsorption on the perfect anatase TiO_2(101) surface: (a) $Ni_{4,a}$; (b) $Ni_{4,b}$; (c) $Ni_{4,c}$; (d) $Ni_{5,a}$; (e) $Ni_{6,a}$.

Figure 10. Top (left) and side views (right) of the stable structures and energies for Ni_4, Ni_5 and Ni_6 adsorption on the defective anatase TiO_2(101) surface: (a) $Ni_{4,A}$; (b) $Ni_{5,A}$; (c) $Ni_{6,A}$.

Figure 11. Cohesive energy of Ni, Au and Pt on the perfect and defective anatase TiO_2(101) surfaces at different cluster sizes.

Figure 12. Variation of $E_{Ni\text{-}TiO2}$ and $E_{Ni\text{-}Ni}$ with the cluster sizes of Ni on the perfect and defective anatase TiO_2(101) surface as well as $E_{Ni\text{-}Ni}$ for bare Ni .

Figure. 1

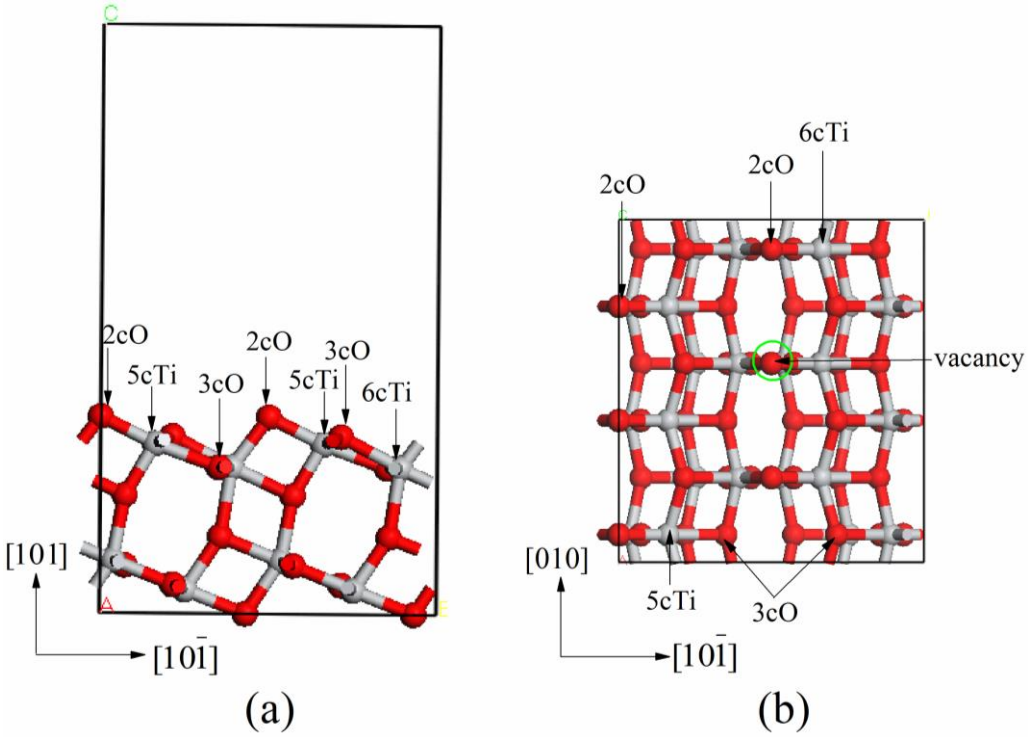

Figure. 2

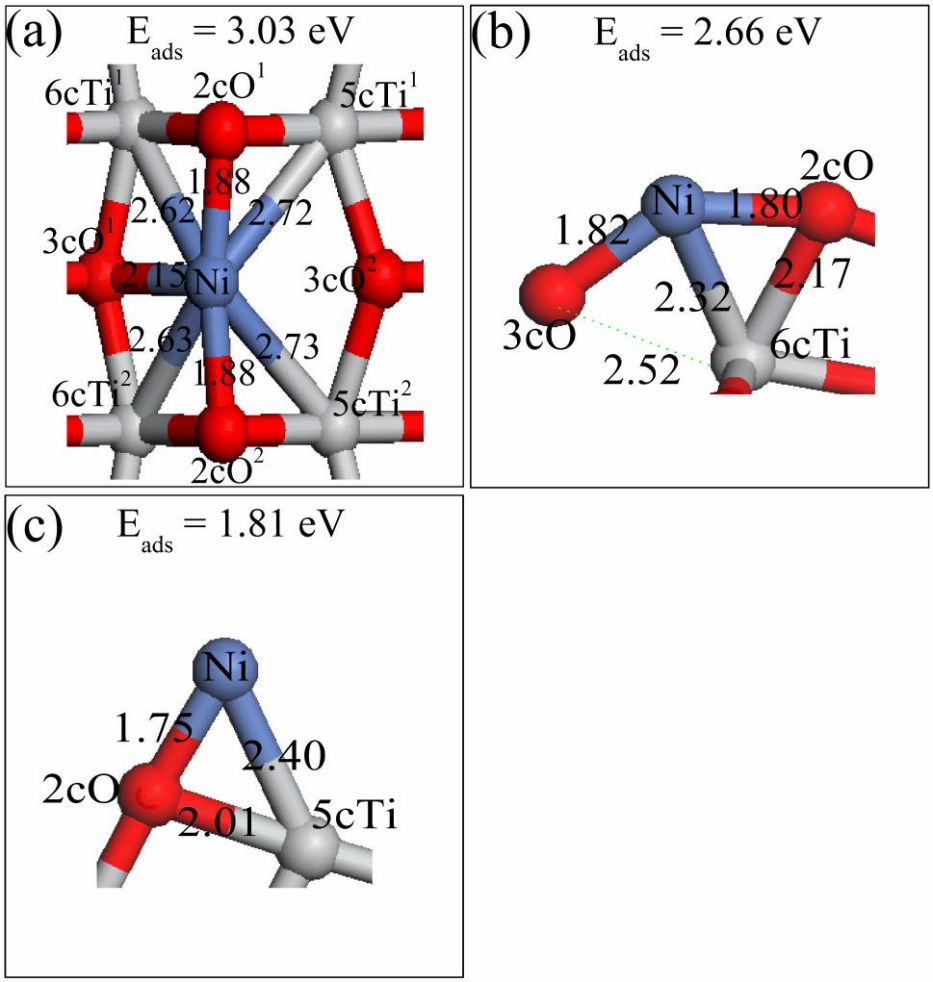

Figure. 3

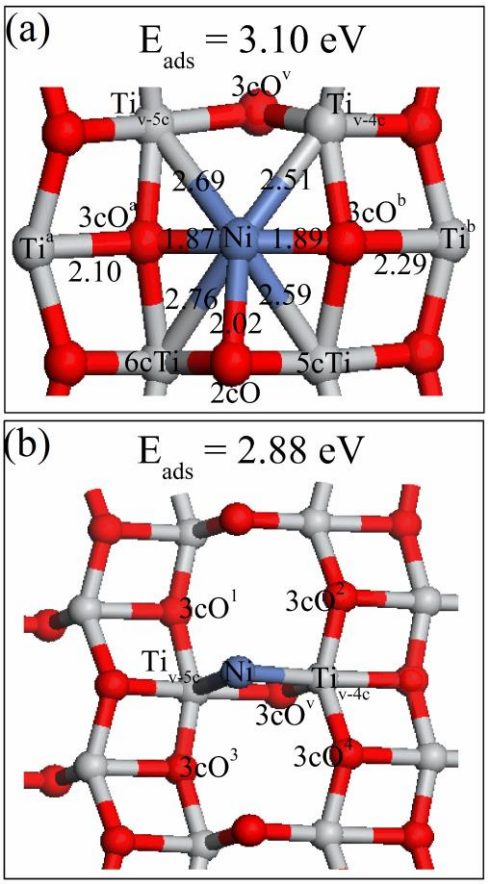

Figure. 4

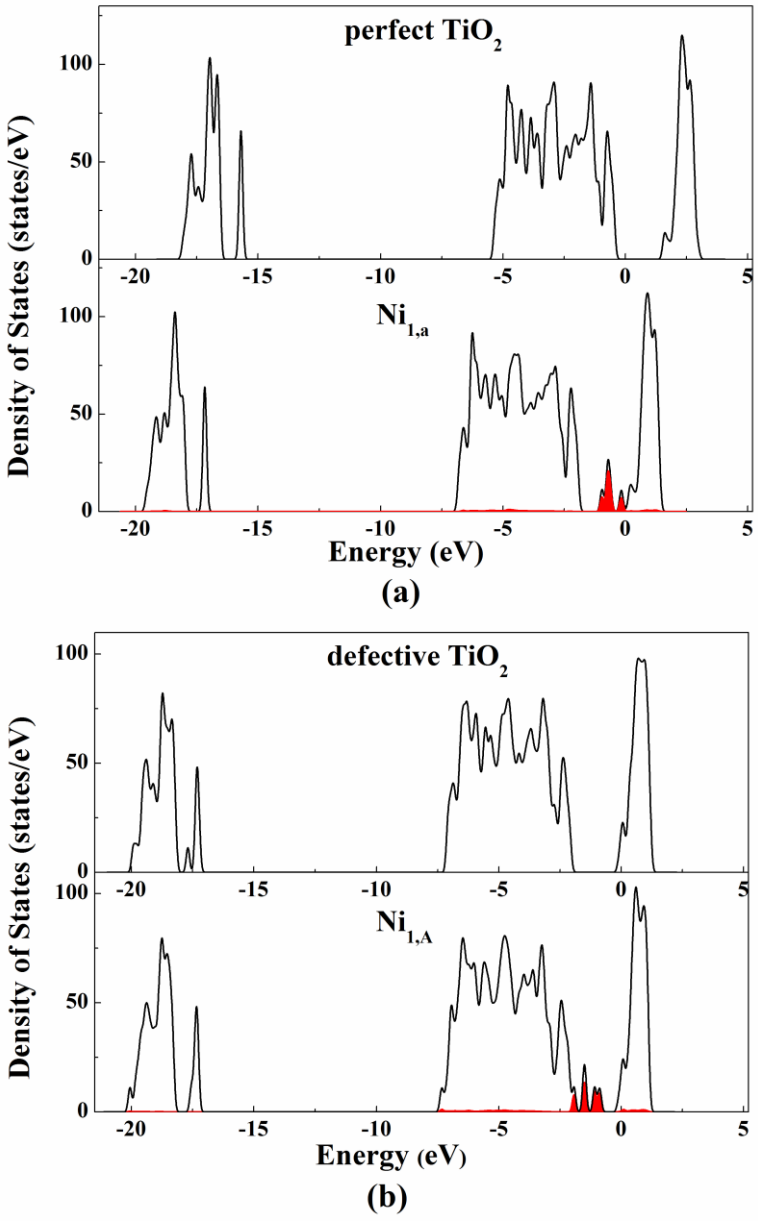

Figure. 5

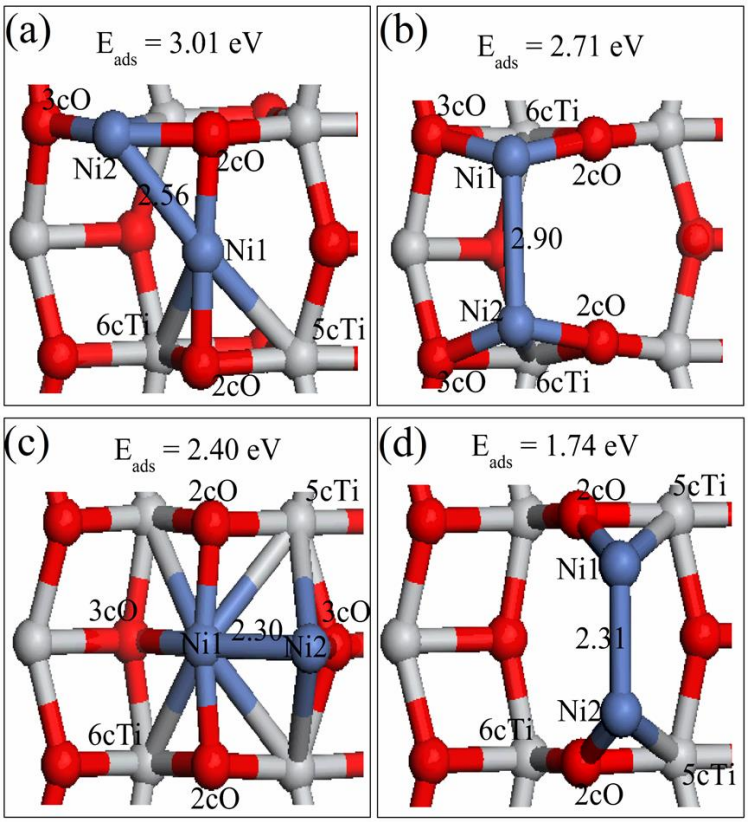

Figure. 6

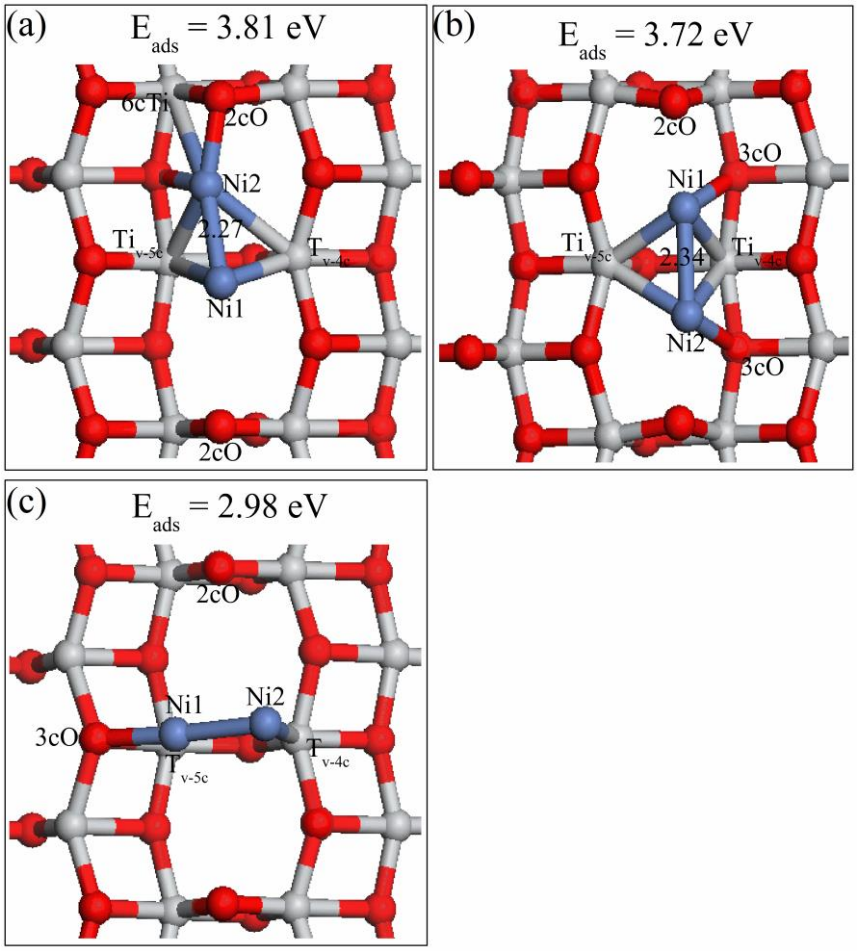

Figure. 7

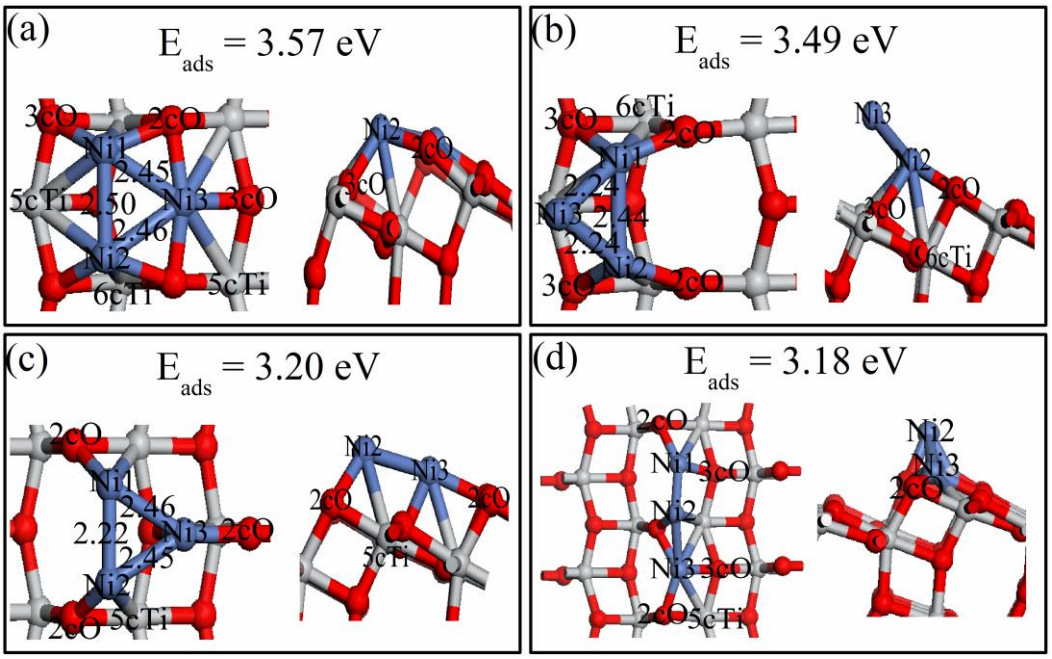

Figure. 8

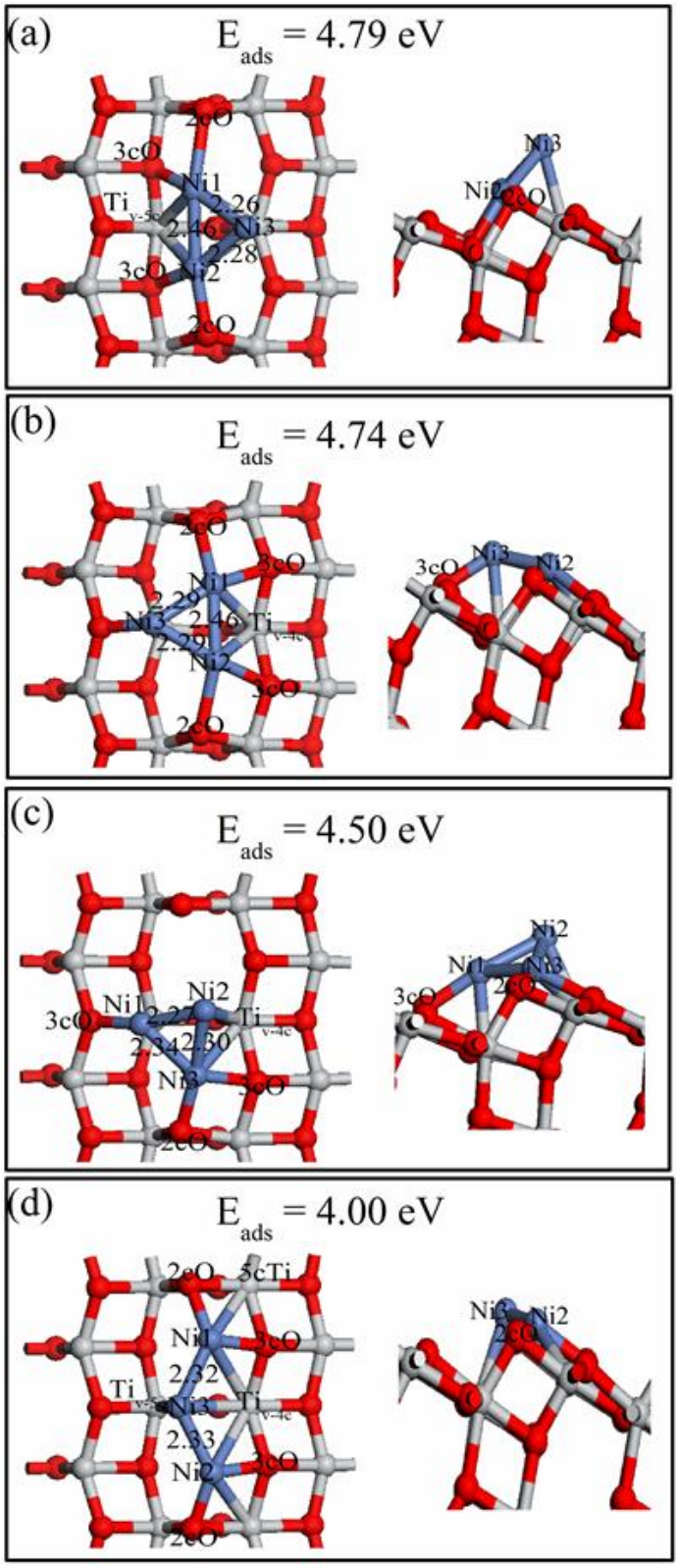

Figure. 9

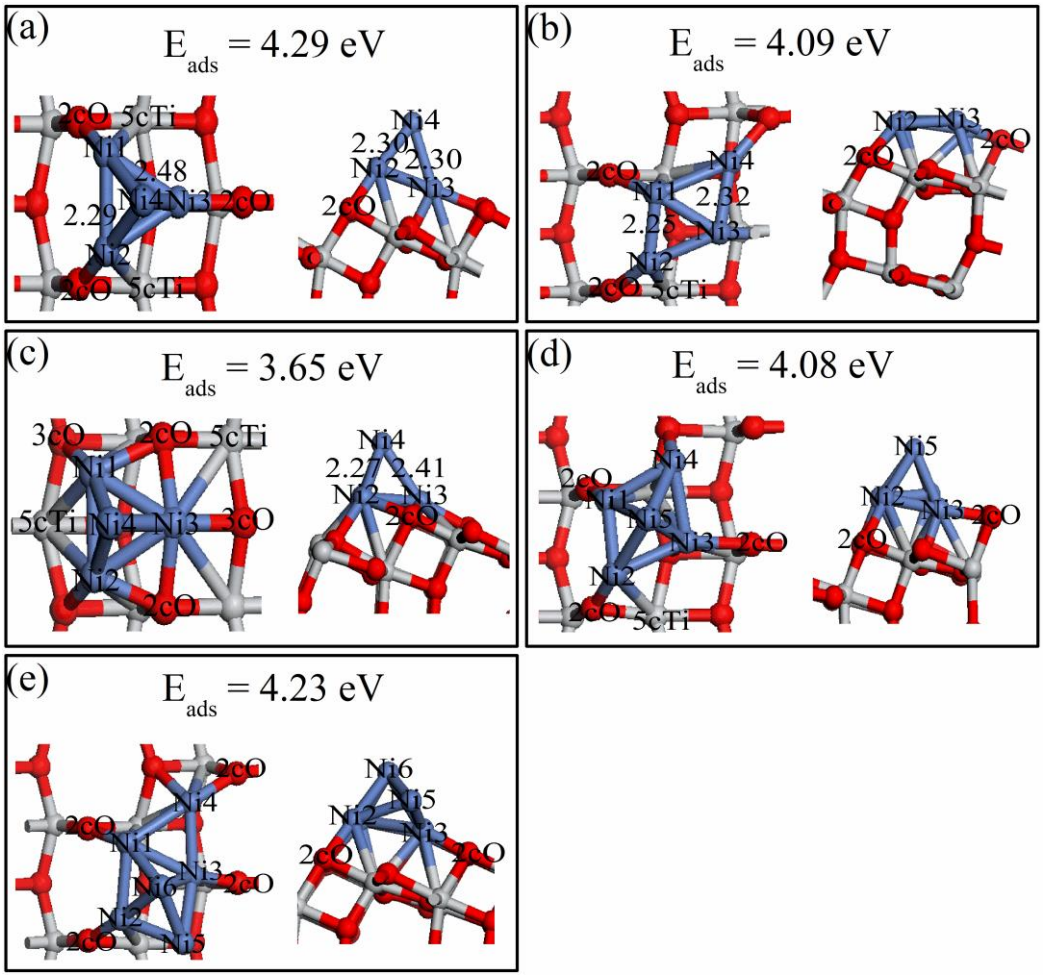

Figure. 10

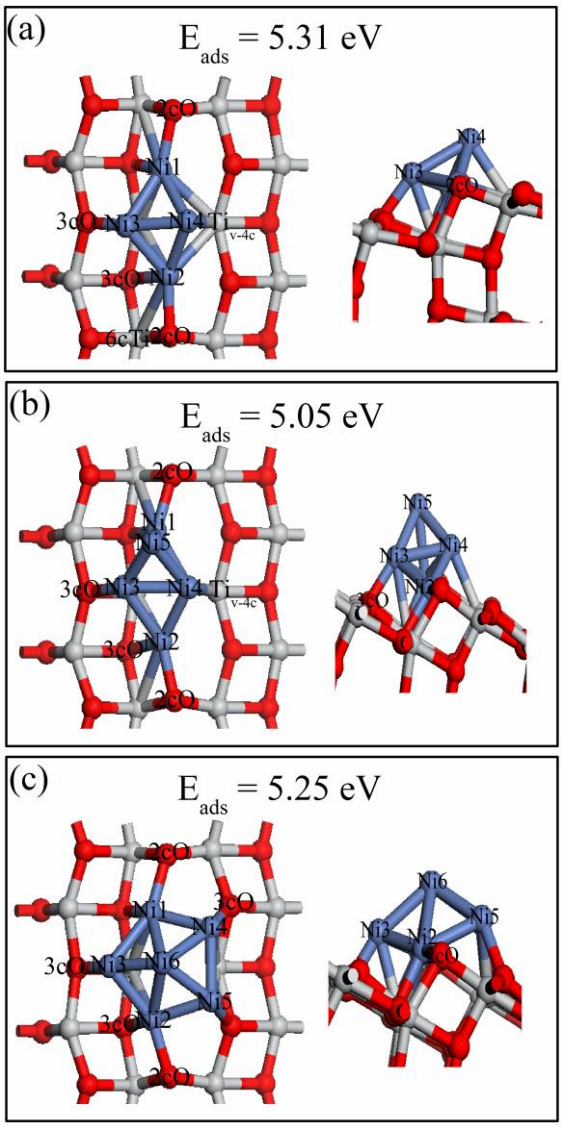

Figure. 11

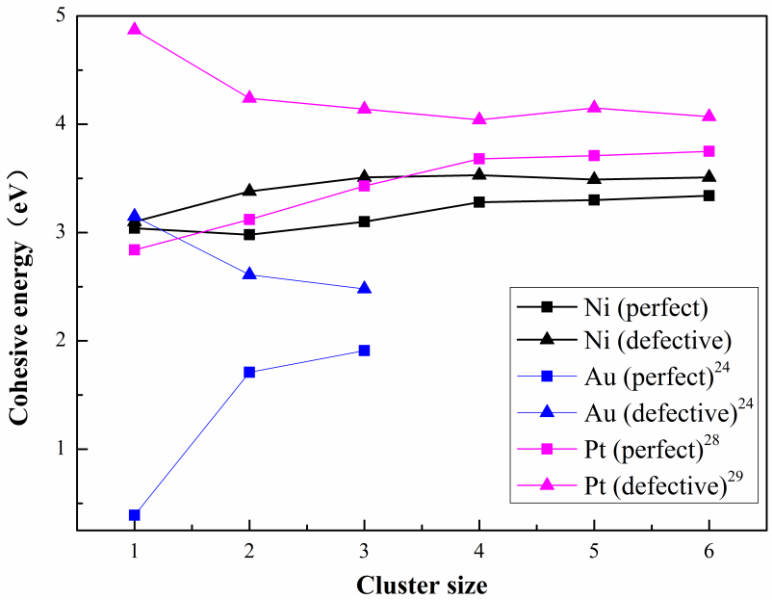

Figure. 12